Hindawi
International Journal of Aerospace Engineering
Volume 2022, Article ID 4633333, 15 pages
https://doi.org/10.1155/2022/4633333

Research Article

Effects of Flow Coefficient on Turbine Aerodynamic Performance and Loss Characteristics

Shaoyun Yang, Wei Du, Lei Luo, and Songtao Wang

School of Energy Science and Engineering, Harbin Institute of Technology, Harbin, China

Correspondence should be addressed to Wei Du; hitdw9211@outlook.com

Received 7 July 2022; Accepted 5 September 2022; Published 16 September 2022

Academic Editor: Hao Chen

Copyright © 2022 Shaoyun Yang et al. This is an open access article distributed under the Creative Commons Attribution License, which permits unrestricted use, distribution, and reproduction in any medium, provided the original work is properly cited.

The effects of flow coefficient on the gas flow and loss characteristics inside the high-pressure turbine is investigated using a numerical simulation. In this paper, the midspan of the first stator of the "Lisa" 1.5 stage high-pressure turbine is used as a prototype to obtain different flow coefficients by changing the stagger angle and the exit angle. The boundary conditions of all cases are consistent with the experimental data of "Lisa". The results show that the flow coefficient is decreased from 0.478 to 0.374 as the stagger angle is varied from 44.2° to 56.2° and from 0.630 to 0.341 as the exit angle is varied from 63° to 75°. Large stagger angle or large exit angle both cause an increase in turbine aerodynamic losses. The similarity between the two is that both cause enhanced effect of transverse secondary flow in the passage. The difference is that with large stagger angle, the adverse pressure gradient affects a large area, resulting in large boundary layer losses; with large exit angle, the passage vortex is weakened but with a large influence area.

1. Introduction

Improving the thrust-to-weight ratio of engines has been a long-standing goal of researchers [1, 2]. On the one hand, the turbine inlet temperature can be increased to increase the thrust, and the turbine inlet temperature has now reached over 1800 K, which requires reliable high temperature resistant materials and effective cooling techniques [3–9]. On the other hand, the turbine load can be increased to reduce the number of blades to reduce the turbine weight [10, 11], but this brings problems related to blade strength. When both methods are difficult to achieve, increasing the flow rate can be used to increase the engine thrust, which means that the turbine has a high flow coefficient. Therefore, it is necessary to study the aerodynamic characteristics and loss distribution inside the turbine for different flow coefficients.

In the early studies, flow coefficient φ and loading coefficient ψ were considered as key design parameters. Smith experimentally established a simple correlation equation between turbine efficiency and flow coefficient and loading coefficient [12]. As the flow coefficient was increased, the turbine efficiency showed a tendency to be increased and then decreased. The efficiency was improved because the development of boundary layer and secondary flow was limited by the high velocity airflow. However, when airflow velocity exceeded a certain range, large dynamic pressure caused a decrease in efficiency.

The Smith chart provided a simple reference for turbine design. To ensure the rationality of the turbine design results, the researchers proposed a large number of loss models. Some of the famous models include Aineley and Mathieson [13], Craig and Cox [14], Kacker and Okapuu [15], etc. Coull et al. compared the completeness of each model's reproduction of the Smith chart and assessed the accuracy of the loss correlations [16]. The results showed that the profile loss model of Coull and Hodson, and the secondary loss model of Craig and Cox predict reasonable results. Coull et al. found higher profile loss at high stage loading coefficient and low flow coefficient, and higher secondary loss at high flow coefficient and low stage loading coefficient. At high flow coefficients, the profile loss showed a weak increasing trend due to increasing Reynolds number, and the secondary loss showed a significant increasing trend

due to higher outlet dynamic pressure. To investigate the influence of the selection of key parameters on the turbine aerodynamic design, researchers have conducted many studies based on the Smith chart through mean line analysis and experiments. Ivan et al. [17] found that the flow coefficient is one of the most critical design parameters affecting the turbine aerodynamic efficiency by mean-line multidimensional optimization. Vázquez et al. compared the advantages and disadvantages of high through-flow design(HTF) and low through-flow design(LTF) in loading low pressure turbines and refined the Smith chart based on the flow characteristics [18]. Vázquez concluded that HTF was similar to conventional blades, resulting in a large exit Mach number. The HTF reduced the blade length, while keeping the flow rate constant, to reduce engine weight and engine size.

Although the Smith chart gives the effects of flow coefficient on turbine efficiency, there is a lack of detailed description of the effects of flow coefficients on the high-pressure turbine flow field. Secondary flow losses are one of the main factors to affect the high-pressure turbine aerodynamic performance. Wang et al. visualized the generation and development of vortex structures such as passage vortices, horseshoe vortices, and shedding vortices by smoke tracing technique [19]. Qu et al. compared the differences of secondary flow structures in the passage of front-loaded and aft-loaded blades [20]. It was found that the transverse secondary flow in the front-loaded blade was stronger without the wake; the development of secondary flow was inhibited with the wake. Qu also discussed the interaction between wake and endwall secondary flow. They found that the wake reduced the end-wall secondary flow losses at higher Reynolds number [21]. Winhart et al. analyzed the complex interactions between the wake, the secondary flow structure and the boundary layer flow to determine the contribution of the secondary flow components to the turbulent kinetic energy [22, 23]. Darji studied the generation location of horseshoe vortices and the development pattern of endwall flow under different working conditions [24]. Tsujita found that the increase in exit Mach number reduced the transverse secondary flow on the endwall, causing weaker passage vortices [25]. Profile losses are also one of main reasons for turbine aerodynamic performance reduction. Simoni et al. studied the effects of wake on profile loss and found that the well-mixed wake caused low profile loss [26]. Kodama et al. proposed a method to estimate profile loss and demonstrated the accuracy of the method by RANS [27]. However, few studies have covered the effect of the flow coefficient on the loss distribution. In order to explain the reason for the decrease in efficiency at high or low flow coefficients, it is necessary to study the effect of flow coefficient on flow structure and loss distribution.

According to the existing literature, the flow coefficient is an important influencing parameter for turbine aerodynamic performance. Although the effect of flow coefficient on efficiency has been studied experimentally and by mean line analysis, there are few studies on the causes of efficiency decrease due to flow coefficient variation. It is necessary to study the effect of flow coefficient on high-pressure turbine secondary flow loss and lobe loss. Therefore, this paper hopes to compare the aerodynamic performance of high-pressure turbine with different flow coefficients by CFD simulation. The effect of the flow coefficient on the flow characteristics within the high-pressure turbine is investigated. Explain the reasons of efficiency decrease by analyzing the magnitude and distribution of losses.

Table 1: Profile geometry parameters.

Parameter	Value
Profile inlet angle	0.0°
Profile exit angle, β	72.0°
Stagger angle, α	50.2°
Axial chord	49.71 mm
Pitch	63.70 mm
Height	70 mm
LE radius	7.00 mm
TE thickness	1.30 mm

Table 2: Studies cases.

Parameter	Baseline	Variation range
Stagger angle, α	50.2°	44.2° to 56.2°
Exit angle, β	72°	63° to 75°

2. General Description of Physical Models

In this study, the differences in loss characteristics and flow structure in a high-pressure turbine guide vane with different flow coefficients are numerically investigated. Considering that the axial velocity at the exit of the turbine is the determining factor of the flow coefficient [28], it is necessary to study the geometrical parameters of the cascade that have an influence on the axial velocity. On the one hand, the stagger angle affects the passage shape, and on the other hand, the exit angle affects the flow rate. Therefore, the flow coefficient is varied by changing the stagger angle or the exit angle. A single row cascade model is used in the study. The model is based on the midspan of the first stator of the "Lisa" 1.5 stage high-pressure turbine. Table 1 shows the geometric parameters. The software Autoblade is used to change the stagger angle and the exit angle while other parameters, such as the axial chord, remain unchanged. Table 2 Shows the cases. Figure 1. shows the parameters definition and the cascade geometry of some cases.

3. Computational Details

3.1. Overview. The commercial software ANSYS CFX, which uses the element-based finite volume, is used to predict the flow structure in the cascade passage. The Shear Stress Transport $\gamma - \theta$ turbulence model is used to solve the three-dimensional constant turbulence flow. The grid is generated using Autogrid5. The boundary condition parameters are obtained from Behr [29].

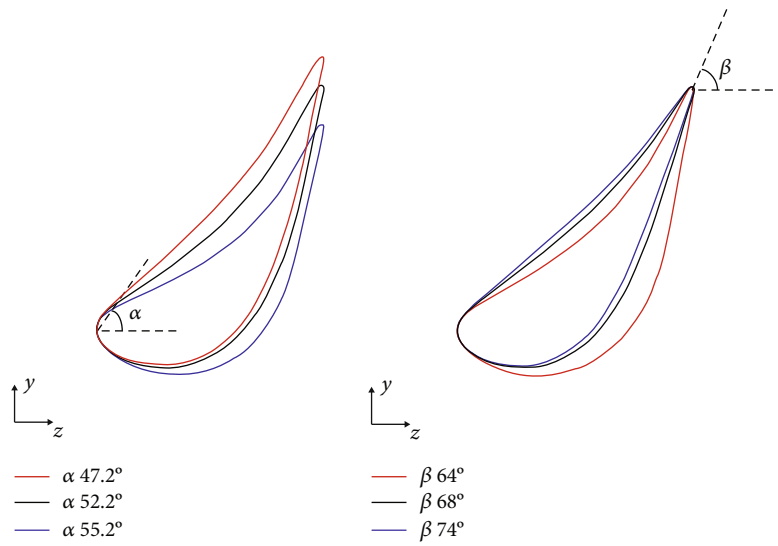

Figure 1: Parameters definition.

3.2. Control Equations. In this paper, the RANS model is used for the steady simulation, whose control equations are shown below.

$$\frac{\partial \rho}{\partial t} + \frac{\partial}{\partial x_j}\left(\rho \bar{u}_j\right) = 0 \tag{1}$$

$$\frac{\partial}{\partial t}\left(\rho \bar{u}_i\right) + \frac{\partial}{\partial x_j}\left(\rho \bar{u}_i \bar{u}_j\right) = -\frac{\partial p}{\partial x_i} + \frac{\partial}{\partial x_j}\left[\mu\left(\frac{\partial \bar{u}_j}{\partial x_i} + \frac{\partial \bar{u}_i}{\partial x_j}\right) - \rho\overline{u_i' u_j'}\right] - \frac{2}{3}\frac{\partial}{\partial x_j}\left(\mu\frac{\partial \bar{u}_j}{\partial x_i}\right) \tag{2}$$

$$\frac{\partial}{\partial t}\left(\rho c_p \bar{T}\right) + \frac{\partial}{\partial x_j}\left(\rho c_p \bar{u}_j \bar{T}\right) = \frac{\partial}{\partial x_j}\left[\frac{\mu}{\mathrm{Pr}}\frac{\partial}{\partial x_j}\left(c_p \bar{T}\right) - \rho c_p \overline{x_j' T'}\right] + S_E \tag{3}$$

3.3. Parameter Definitions. The flow coefficient is defined as [29]:

$$\varphi = \frac{\mathrm{c_x}}{\mathrm{u}} \tag{4}$$

where here c_x is the axial velocity of the airflow at the outlet of the guide vane, u is the blade velocity at midspan.

The aerodynamic performance of turbine blade is commonly measured by the total pressure loss coefficient. The total pressure loss coefficient is defined as:

$$\mathrm{Y} = \frac{\mathrm{p_{t,in}} - \mathrm{p_{t,out}}}{\mathrm{p_{t,out}} - \mathrm{p_{s,out}}} \tag{5}$$

Where here $p_{t,\mathrm{in}}$ is the inlet total pressure, $p_{t,\mathrm{out}}$ is the outlet total pressure, $p_{s,\mathrm{out}}$ is the outlet static pressure.

C_p is a commonly used result of the dimensionless treatment of static/total pressure, which is defined by

$$\mathrm{C_p} = \frac{\mathrm{p} - \mathrm{p_{s,out}}}{\mathrm{p_{t,inlet}} - \mathrm{p_{s,out}}} \tag{6}$$

In the case of the total pressure coefficient C_{pt}, the pressure is taken as the measured value of the total pressure, and in the case of C_{ps}, the pressure is taken as the static pressure.

The dissipation function ϕ characterizes the irreversible loss of mechanical energy during fluid flow and is defined by the following equation [30]:

$$\frac{\phi}{\mu} = 2\left[\left(\frac{\partial u}{\partial x}\right)^2 + \left(\frac{\partial v}{\partial y}\right)^2 + \left(\frac{\partial w}{\partial z}\right)^2 + \left(\frac{\partial v}{\partial x} + \frac{\partial u}{\partial y}\right)^2 + \left(\frac{\partial w}{\partial y} + \frac{\partial v}{\partial z}\right)^2 + \left(\frac{\partial u}{\partial z} + \frac{\partial w}{\partial x}\right)^2\right] - \frac{2}{3}\left(\frac{\partial u}{\partial x} + \frac{\partial v}{\partial y} + \frac{\partial w}{\partial z}\right)^2 \tag{7}$$

Where here μ is the dynamic viscosity.

The boundary layer momentum thickness θ is defined as the thickness of the mainstream corresponding to momentum loss of the boundary layer, which approximates the loss caused by the boundary layer, and the definition equation is shown below.

$$\theta = \int_0^{\delta} \frac{\rho \mathrm{u}}{\rho_e \mathrm{u_e}}\left(1 - \frac{u}{u_e}\right) dy \tag{8}$$

Where here δ is the thickness of the boundary layer, ρ is the local density of the boundary layer, u is the local tangential velocity in the boundary layer, ρ_e is the mainstream density, u_e is the mainstream velocity.

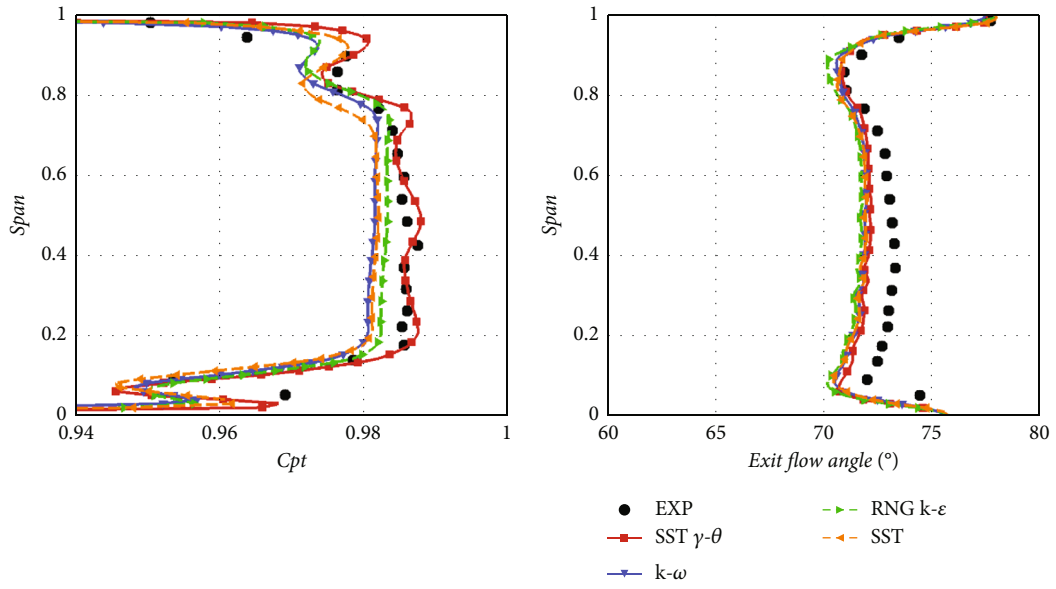

(a) Total pressure coefficient (b) Exit Flow Angle

Figure 2: Comparison between the numerical results and experimental results.

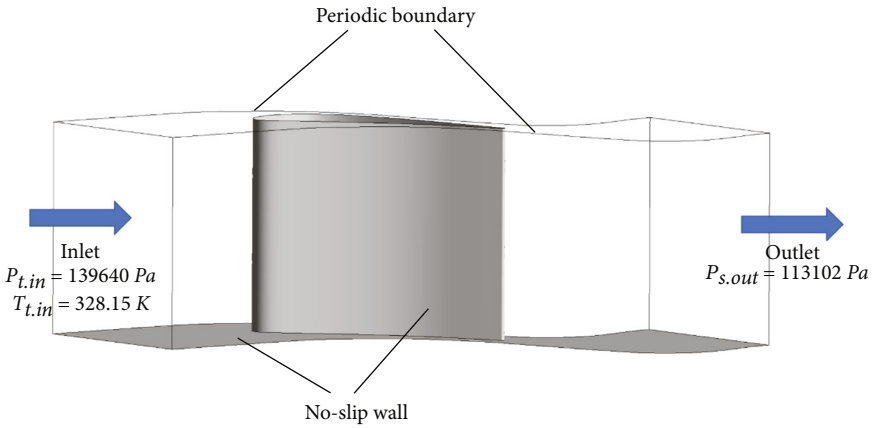

Figure 3: Computational domain and boundary conditions.

3.4. Turbulent Model Selection. The experimental results from the Behr [29] are compared with the numerical results, which is obtained by four different turbulence models, as shown in Figure 2. The boundary conditions of the four cases, such as the total inlet pressure, the total inlet temperature and the static outlet pressure, are consistent with the experimental boundary conditions given in the reference [29]. Figure 2(a) shows that the trends of the total pressure coefficient along the blade predicted by these four turbulence models are similar to the experimental results. The shear-stress-transport (SST), $k-\omega$ and RNG $k-\varepsilon$ turbulence under-predict the total pressure coefficient. The predicted value of SST $\gamma-\theta$ turbulence model is more accurate compared to the other models. Figure 2(b) shows that all models under-predict the exit airflow angle compared to the experimental results, but the trends of the predicted results are consistent with the experimental ones. And it is found that the exit airflow angle predicted by SST $\gamma-\theta$ turbulence

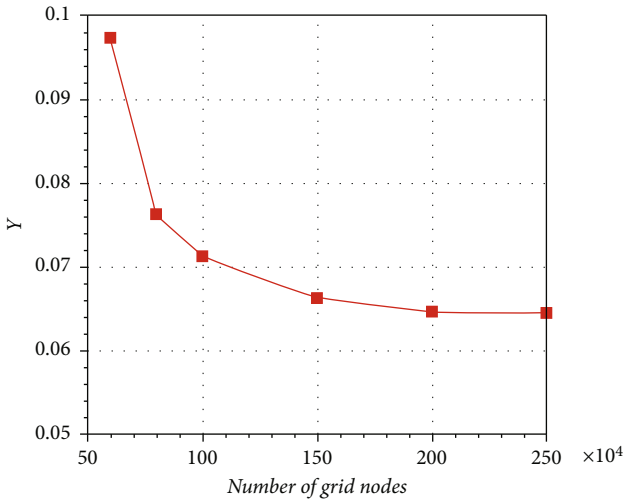

Figure 4: Mesh independence.

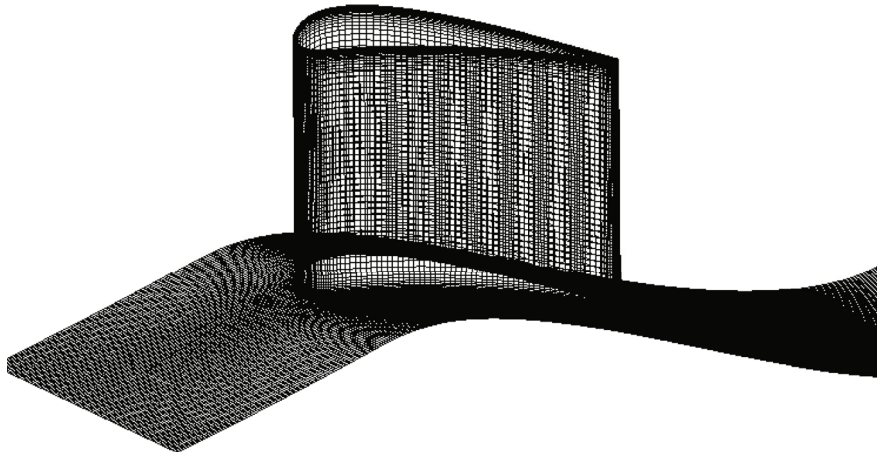

Figure 5: Detail of mesh.

model is closet to the experimental value. By comparing the accuracy of the predicted total pressure coefficient and exit airflow angle, SST $\gamma - \theta$ is found to be the best choice for predicting the aerodynamic performance of the studied blades. Therefore, the SST $\gamma - \theta$ is used to predict the flow state and loss variation in the turbine passage at different flow coefficients in this study.

3.5. Boundary Conditions. Considering the low velocity and pressure in the calculation, ideal gas with constant specific heat capacity and viscosity is used in this study. The boundary conditions for the numerical calculations are obtained from Behr [29]. The total inlet temperature is 328.15 K, the total inlet pressure is 139640 Pa and the static outlet pressure is 113102 Pa. As shown in Figure 3, no-slip boundary conditions are used for the endwall and blade wall. Periodic boundary conditions are used.

3.6. Grid Details and Independent Solutions. In this study, the structured meshes are generated by Autogrid5. This is an automatic turbomachine mesh generation program provided by Numeca. The grid adopts O4H topology. The main flow passage grid adopts H-type topology and the grid around the blade adopts O-type topology. The y plus on the end wall is about 1 to capture the detailed flow structure. To ensure the accuracy of the calculation results while also minimizing the calculation time, the grid independence is carefully evaluated and the results are shown in Figure 4. The results show that the total pressure loss remains almost constant when the number of grids exceeds 2 million. Therefore, the grid number is chosen to be 2 million for all cases. The grid details are shown in Figure 5.

4. Results and Discussion

4.1. Stagger Angle Effects. Figure 6 shows the effects of the stagger angle variation on turbine flow coefficient and total pressure loss coefficient. The results show that the flow coefficient exhibits a downward trend from 0.478 to 0.374 as the stagger angle is increased from 44.2° to 56.2°. This indicates that the stagger angle has important effects on the flow coefficient. It is also seen that the total pressure loss coefficient is increased with increased stagger angle, from 0.033 to 0.059. According to the previous experience, high flow coefficient causes high profile loss, which deteriorates the turbine efficiency. However, the results in Figure 6 show that low flow coefficient also leads to high total pressure loss.

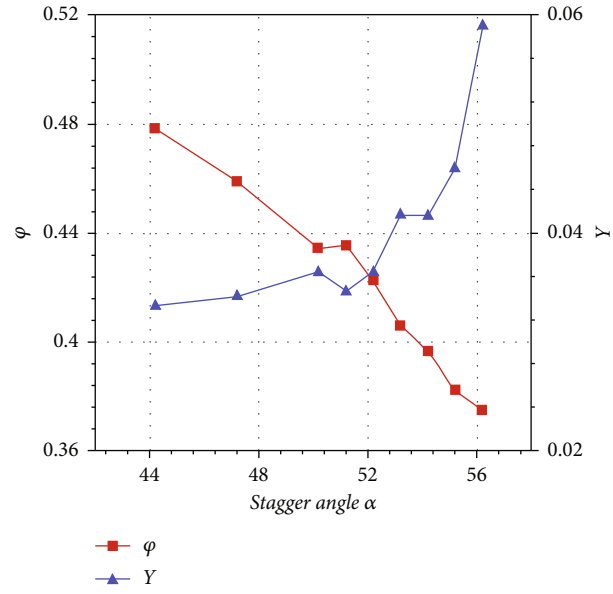

Figure 6: Flow coefficient and total pressure loss coefficient for different stagger angles.

Figure 7 shows the comparison of the static pressure coefficients distribution near the mid-span of the turbine cascades with different stagger angles. As the stagger angle is changed rom 47.2° to 52.2°, the lowest static pressure point moves downstream and the lowest pressure value increases, indicating a decrease in the adverse pressure gradient. This leads to a weak transverse. Then, the lowest static pressure point moves toward the middle and the lowest pressure value gradually decreases as the stagger angle is changed

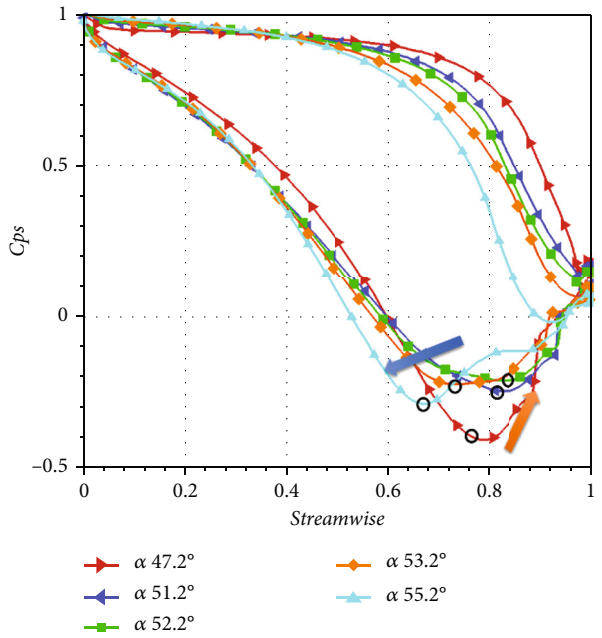

Figure 7: Comparison of static pressure coefficient near the midspan of the blade for different stagger angles.

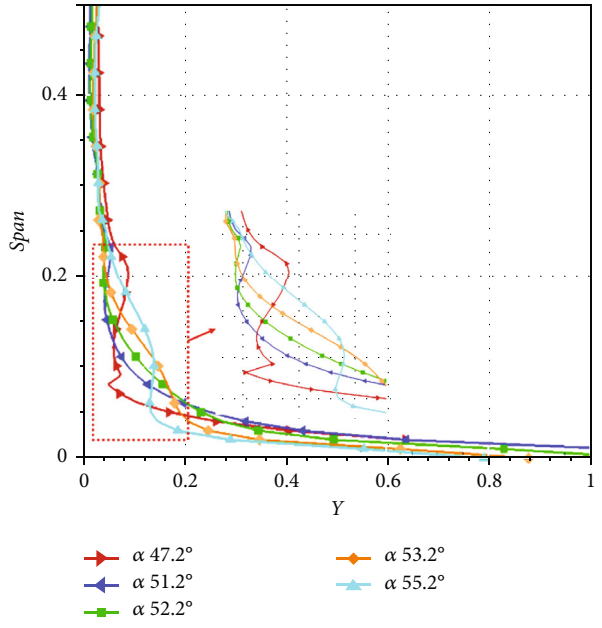

Figure 8: Comparison of total pressure loss coefficient for different stagger angles.

from 52.2° to 55.2°.It shows that the influence range of transverse secondary flow increases. The distribution position of the load does not move backward all the time with the increase of the stagger angle, but moves downstream to a certain position first and then moves to the middle. In addition, the blade load is reduced as the stagger angle is increased.

Figure 8 shows the comparison of the total pressure loss coefficient distribution at the outlet along the span with different stagger angles. The total pressure loss remains constant from 30% to 50% span, then changes due to the passage vortex and endwall secondary flow within the 30% span from the endwall. The loss peak and the influence area of the passage vortex are reduced as the stagger angle is increased from 47.2° to 55.2°. Also, the loss area of the passage vortex moves upward along the span. In contrast, the loss area due to endwall secondary flow is increased as the stagger angle is increased. When the stagger angle is 55.2°, only the influence of the endwall secondary flow is seen. The results show that the increase in the stagger angle

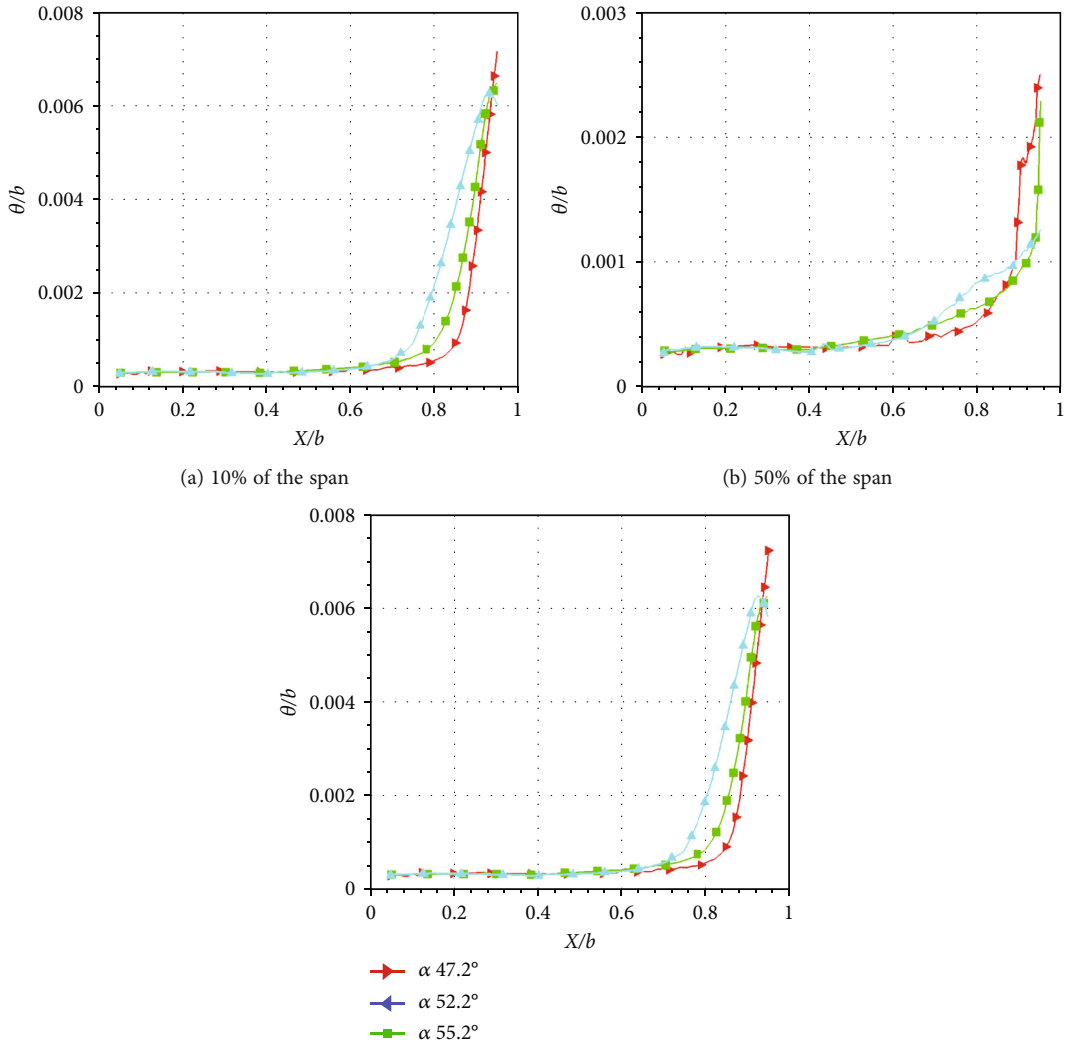

(a) 10% of the span

(b) 50% of the span

(c) 90% of the span

Figure 9: Comparison of boundary layer momentum thickness for different stagger angles.

weakens the passage vortex and enhances the endwall secondary flow.

Figure 6 has shown that the increase in the stagger angle would cause a decrease in the turbine flow coefficient and an increase in the total pressure loss. In order to further analyze the effects of stagger angle variation on the aerodynamic performance of the turbine and the distribution of turbine loss at different flow coefficients, α47.2°, α52.2° and α55.2° are selected to compare the differences in boundary layer momentum thickness, dissipation function, end wall flow lines and total pressure loss at the outlet.

The momentum thickness approximates the loss of boundary layer [31, 32]. Figure 9 compares the boundary layer momentum thickness at different spans for α47.2°, α52.2° and α55.2°. As shown in Figure 9(a), there is no significant change in the boundary layer momentum thickness until 0.6b at 10% span. At 0.6b, the momentum loss of α55.2° is increased under the effect of the adverse pressure gradient, leading to a significant increase in the momentum thickness. α52.2° at 0.75b, α47.2° at 0.8b. In the range from 0.6b to 0.9b, the momentum thickness of α55.2° is the largest among the three cases, indicating that its boundary layer loss is the largest. After 0.9b, the momentum thickness of α47.2° is the largest, indicating that the boundary layer loss near the trailing edge is decreased with increased stagger angle. According to Figure 9(b), the locations where the momentum thickness starts to change significantly are α47.2° at 0.78b α52.2° at 0.8b and α55.2° at 0.65b, which are consistent with the locations of the adverse pressure gradient shown in Figure 7. Figure 9(c) shows similar results to Figure 9(a). The increase in the stagger angle enhances the boundary layer loss in the middle and rear of the cascade and weakens the boundary layer loss near the trailing edge.

The dissipation function is often used to measure the loss of mechanical energy [30]. Figure 10 shows the dissipation function from 0.2b to 0.95b cross sections at α47.2°, α 52.2° and α55.2°. The profile losses near the surface of the

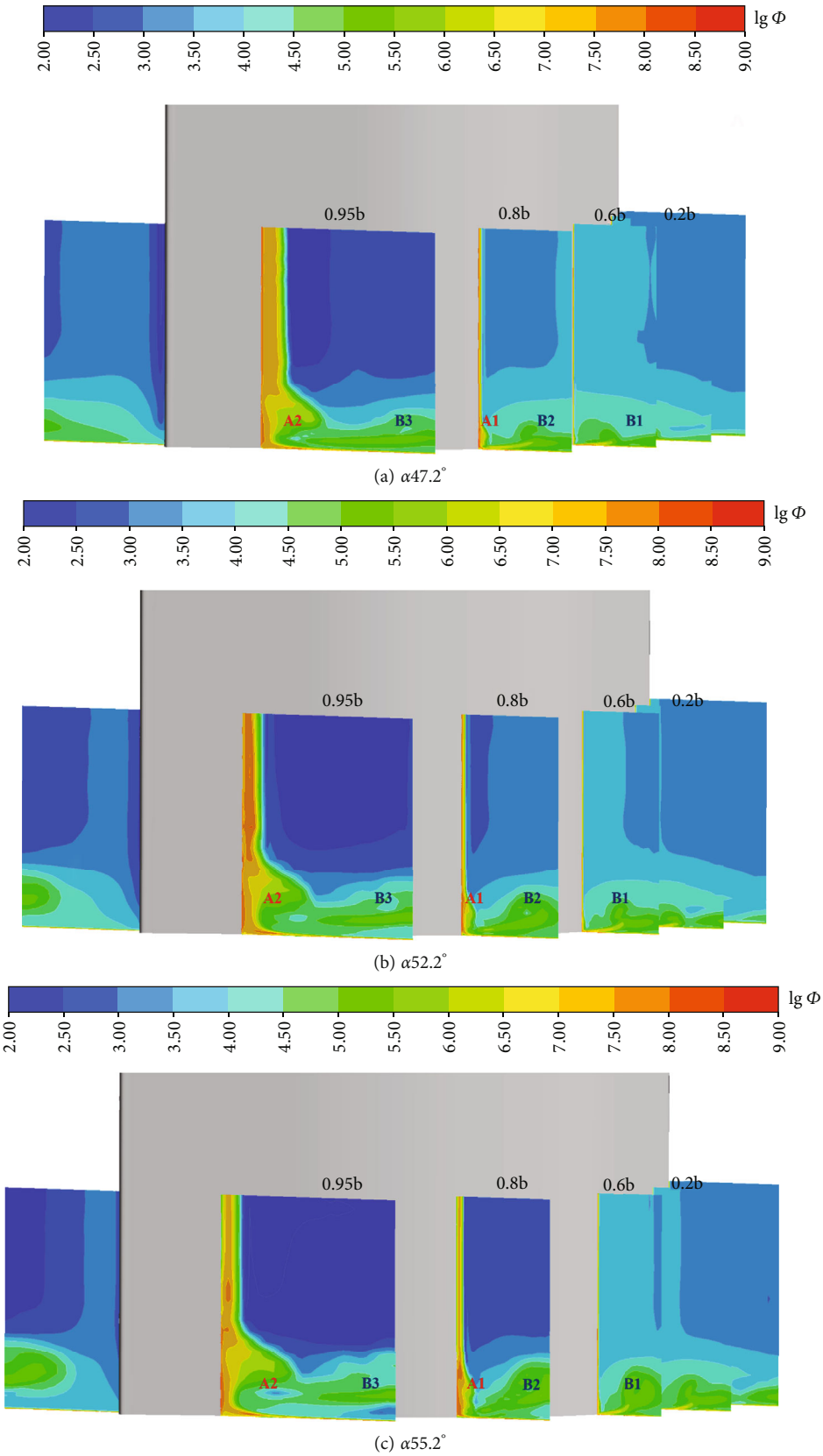

Figure 10: Comparison of dissipation functions for different stagger angles.

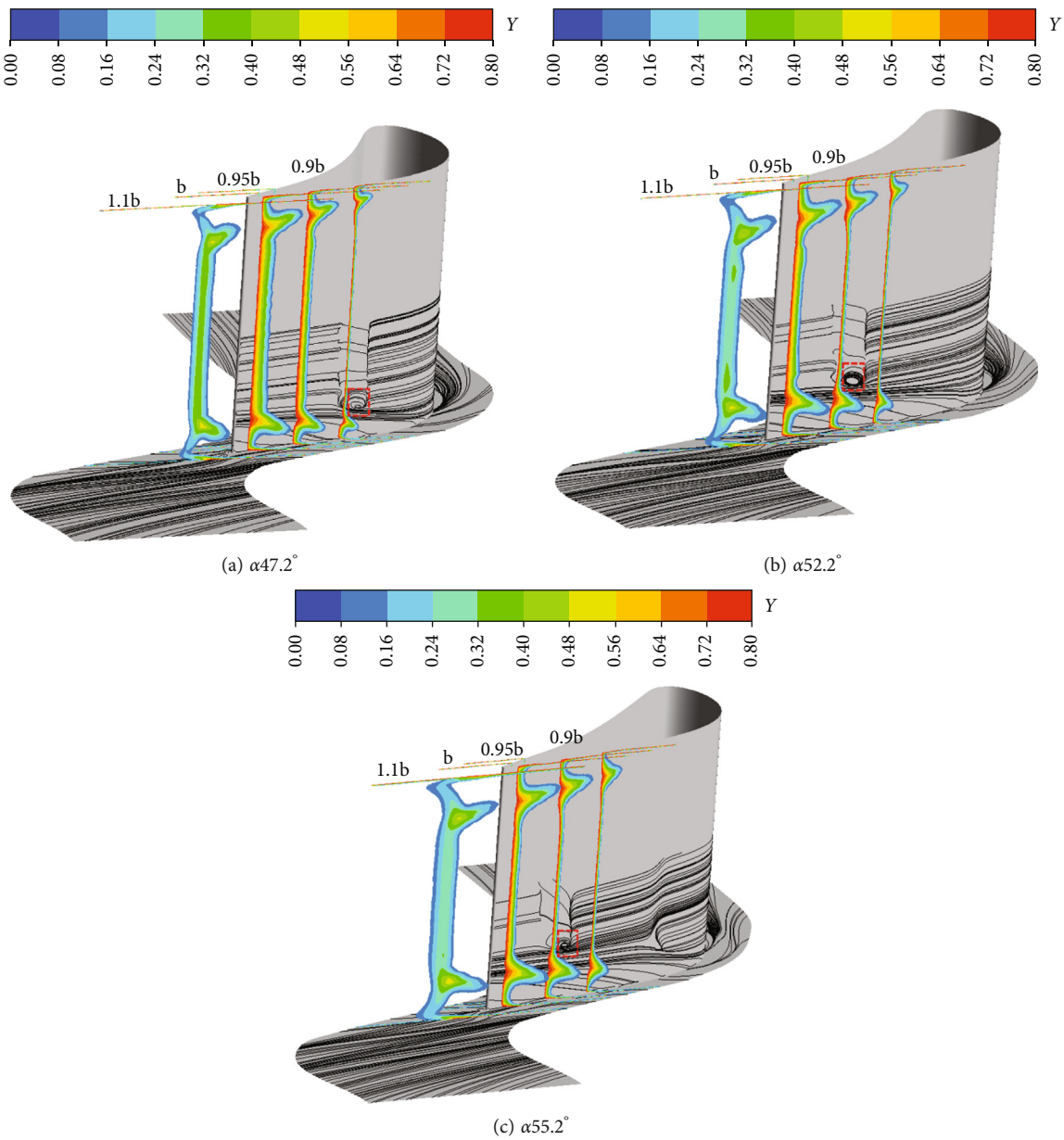

Figure 11: Comparison of total pressure loss and endwall streamline for different stagger angles.

blade body, the losses caused by the passage vortex near the end wall, and the losses caused by the transverse secondary flow in the middle of the passage can be found. The values and distribution characteristics of the dissipation functions vary with the stagger angle. First, the dissipation coefficient near the blade is decreased as the stagger angle is increased at 0.95b, indicating that the profile loss near the trailing edge is decreased. This is consistent with the results of the boundary layer momentum thickness variation shown in Figure 9. The high loss areas of passage vortex and endwall secondary flow loss are indicated by A1 and A2, and the high loss areas of transverse secondary flow are indicated by B1, B2 and B3. Compared with $\alpha 47.2^{\circ}$ and $\alpha 52.2^{\circ}$, $\alpha 55.2^{\circ}$ has relatively larger values of the dissipation function at A1 and A2, indicating that the increase of the stagger angle enhances the losses caused by the passage vortex. Similarly, the dissipation functions at B1, B2, and B3 indicate that increasing the stagger angle also enhances the effect of transverse secondary flow. The high loss region caused by the transverse secondary flow is increased and moved up toward the center of the passage.

Figure 11 shows the total pressure loss coefficient from 0.9b to 1.1b cross sections and the endwall streamline for different stagger angles. The results show that the influence area of passage vortex is reduced with increased stagger angle. Considering that the cascade at $\alpha 47.2^{\circ}$ has a larger flow coefficient, the increase of axial velocity suppress the effect of passage vortices. The distribution of endwall streamline shows that flow separation occurs at the suction surface, whose location gradually moves

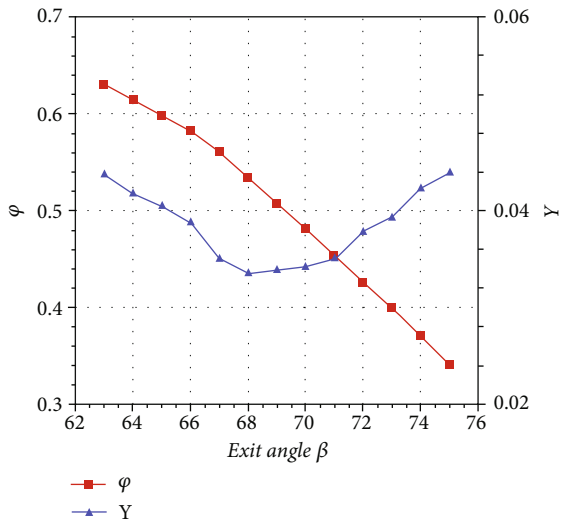

Figure 12: Flow coefficient and total pressure loss coefficient for different exit angles.

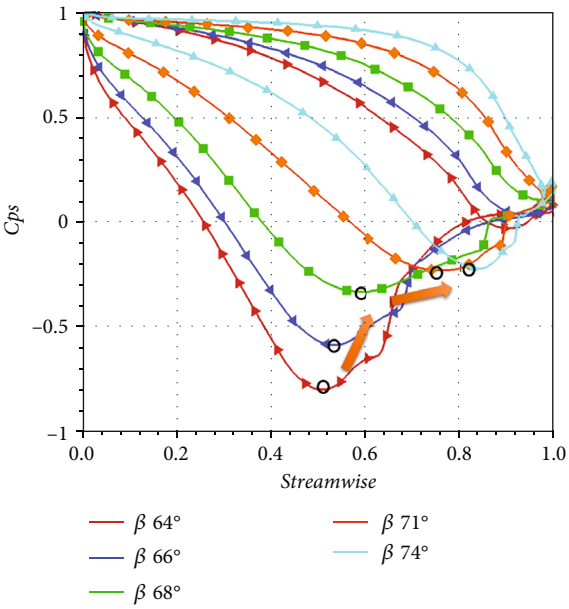

Figure 13: Comparison of static pressure coefficient near the midspan of the blade for different exit angles.

backward with increased stagger angle. This is consistent with the location of boundary layer separation shown in Figure 9(b). In addition, the radial migration of the fluid at the suction surface occurs at α55.2°. The appearance of radial pressure gradients indicates the accumulation of low-energy fluids at the end walls, which enhances secondary flow losses.

4.2. Exit Angle Effect. The axial velocity at the exit of the guide vane is the determining parameter of the flow coefficient, while the exit velocity is determined by the exit angle. In order to analyze the effect of flow coefficient variation on turbine efficiency more comprehensively, the aerodynamic performance of cascade with different exit angles is investigated. Figure 12 shows the variation of the flow coefficient and total pressure loss of the cascade with different exit angles. Comparing with Figure 6, it is found that the flow coefficient is more sensitive to the variation of the exit angle. The flow coefficient is decreased from 0.630 to 0.341 as the exit angle is increased from 63° to 75°. Also, different from the effect caused by the increased stagger angle, the total pressure loss coefficient is first decreased and then increased with the increased exit angle.

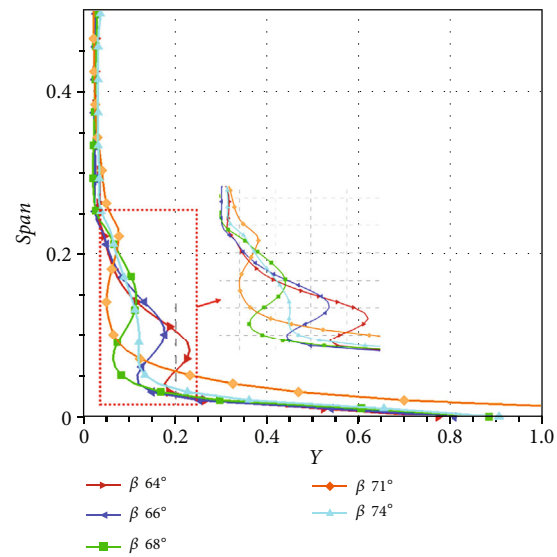

Figure 14: Comparison of total pressure loss coefficient for different exit angles.

Figure 13 shows the comparison of the static pressure coefficients distribution near the mid-span of the turbine cascades with different exit angles. The adverse pressure gradient is decreased and the position of the lowest pressure point at the suction moves from 0.5b to 0.85b as the exit angle is increased from 64° to 74°. When the exit angle is 64°, the suction surface is under the influence of a large adverse pressure gradient from the middle to the trailing edge. It shows that at large exit angle, there is not only strong transverse secondary flow in the passage but also large scale separation at the suction surface.

Figure 14 shows the comparison of the distribution of the total pressure loss coefficient at the outlet along the span for different exit angles. The effects of the change in exit angle on the passage vortex and the endwall secondary flow are different. The loss caused by the passage vortex is decreased with the increase of the exit angle, while the spreading influence area of the endwall secondary flow is increased. When the exit angle is 74°, there is no obvious peak loss of passage vortex, and the endwall secondary flow has a large effect within the 30% span from the endwall. At small exit angle, the loss of passage vortex is large; at large exit angle, the loss of end wall secondary flow is large; when the exit angle is at the suitable value, the effects of both are

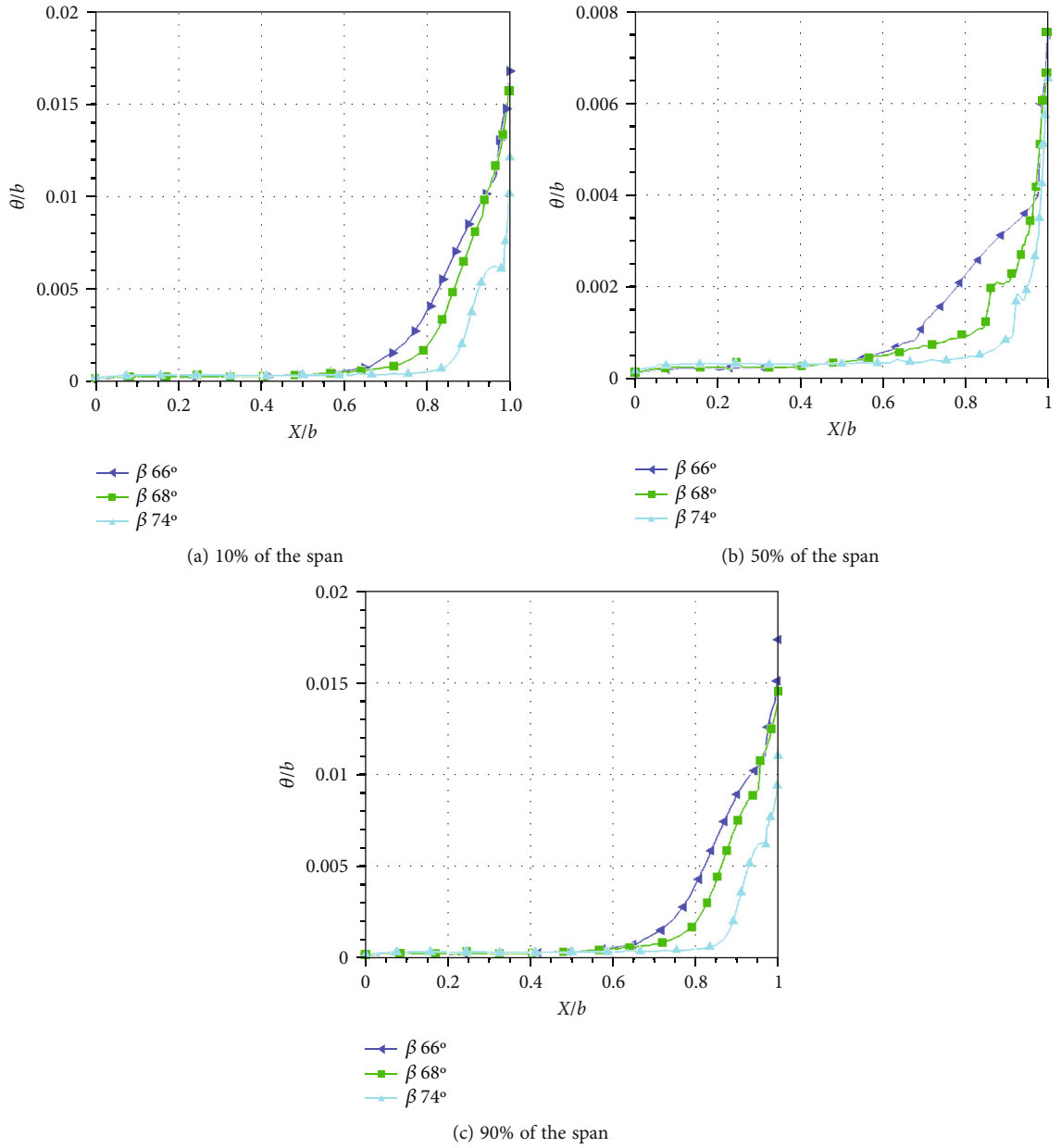

FIGURE 15: Comparison of boundary layer momentum thickness for different exit angles.

small. This corresponds to the variation of the total pressure loss in Figure 7.

Figure 15 compares the boundary layer momentum thickness at different spans for $\beta 66^\circ$, $\beta 68^\circ$ and $\beta 74^\circ$. As shown in Figure 15(a), there is no significant change in the momentum thickness until 0.6b at 10% span. The momentum thicknesses of $\beta 66^\circ$ and $\beta 68^\circ$ increase significantly due to the adverse pressure gradient at 0.6b, with $\beta 66^\circ$ having a faster growth rate. The momentum thickness of $\beta 74^\circ$ is increased at 0.85b. Therefore, the momentum thickness of $\beta 66^\circ$ is the largest among the three cases from 0.6b to 1b, indicating that it has the largest boundary layer loss. Figure 15(b) and Figure 15(c) show a similar pattern to Figure 15(a). Compared with Figure 13, it is found that the size and location of the adverse pressure gradient determine the boundary layer loss. The boundary layer loss is decreased as the exit angle is increased. Comparing the trend of boundary layer loss and secondary flow loss, and considering the trend of total pressure loss coefficient in Figure 12, it could be assumed that the secondary flow loss causes more influence.

Figure 16 shows the dissipation function from 0.2b to 0.95b cross sections at $\beta 66^\circ$, $\beta 68^\circ$ and $\beta 74^\circ$. A1, A2 indicate the high loss region of passage vortex and endwall secondary flow. B1, B2 and B3 indicate the high loss region of transverse secondary flow. By comparison, it is found that the passage vortex loss is decreased and the endwall secondary flow loss is increased with the increase of exit angle at A1. The loss region is reduced at A2. The variation of transverse secondary flow at B2 and B3 is

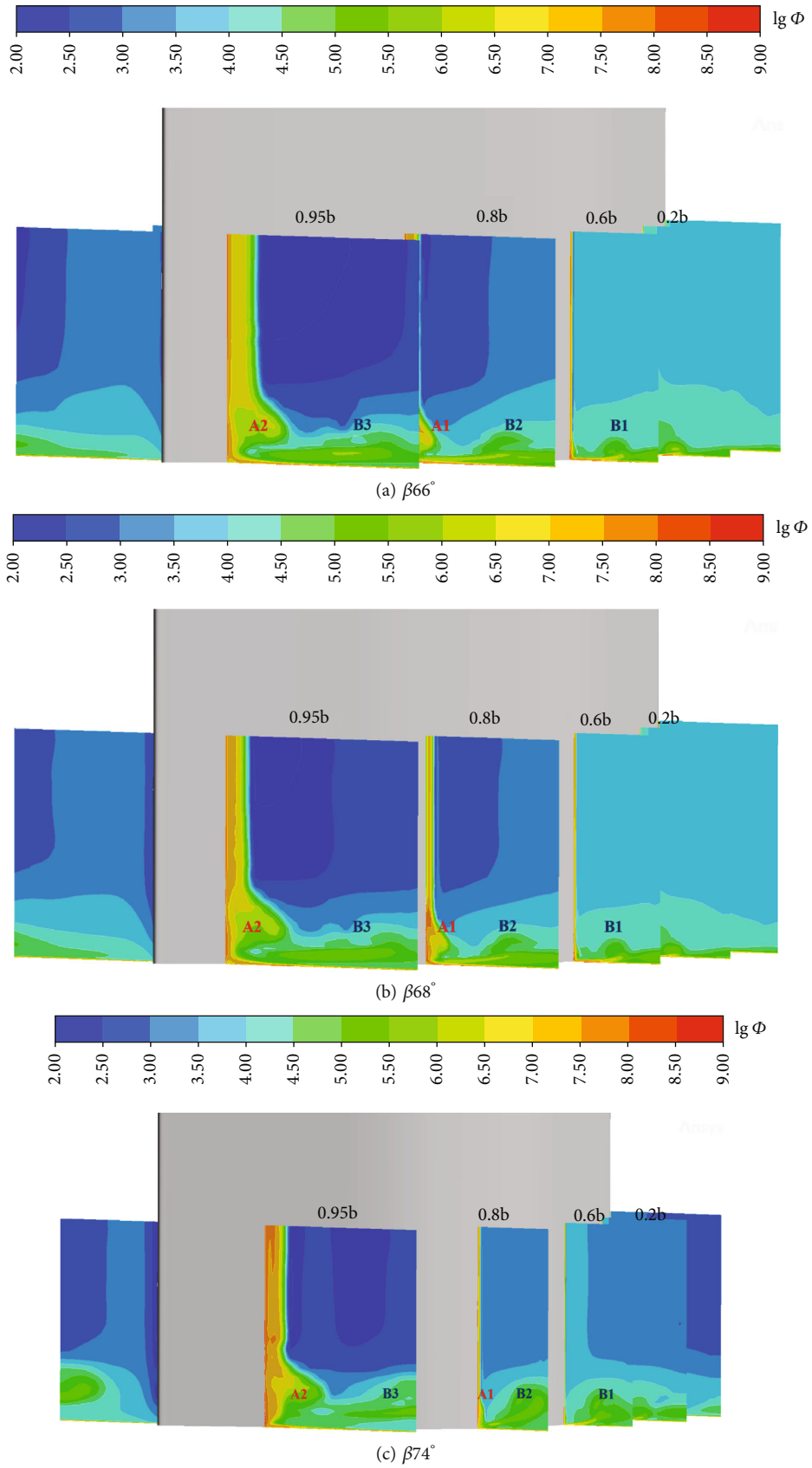

(a) $\beta 66^{\circ}$

(b) $\beta 68^{\circ}$

(c) $\beta 74^{\circ}$

Figure 16: Comparison of dissipation functions for different exit angles.

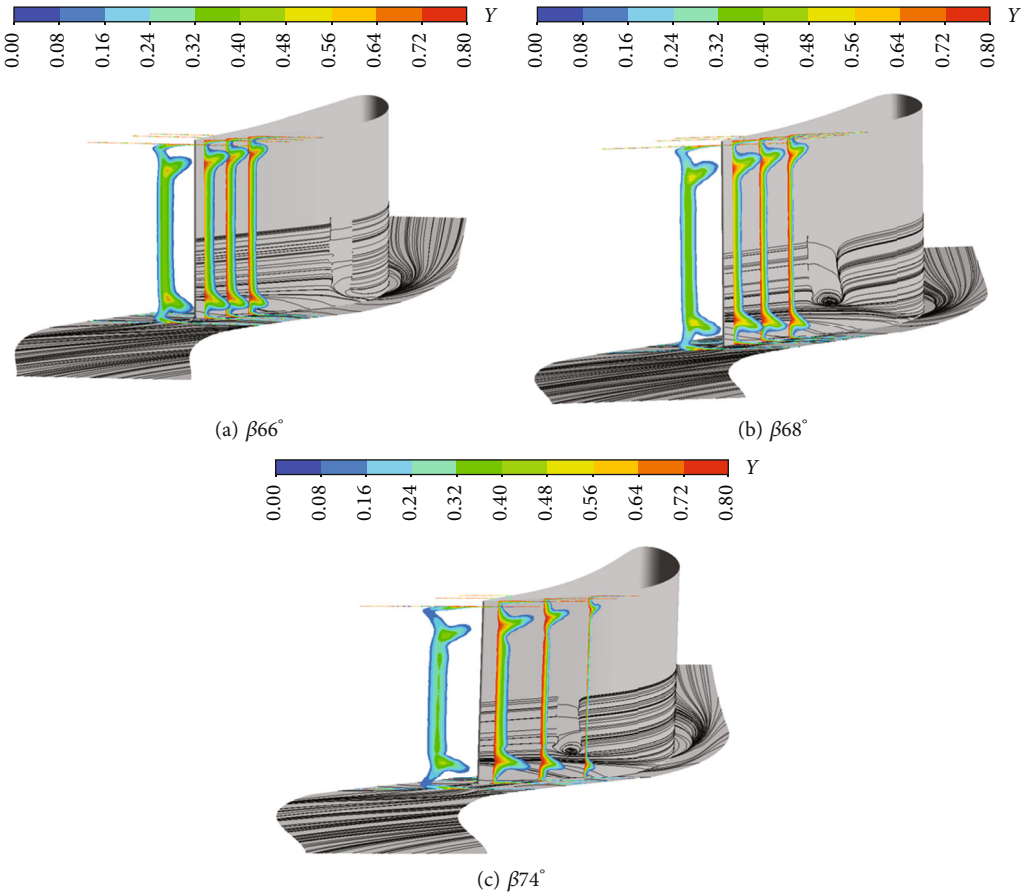

Figure 17: Comparison of total pressure loss and endwall streamline for different exit angles.

worth to note. $\beta 66^{\circ}$ has strong transverse secondary flow, with a small influence area near the endwall. $\beta 74^{\circ}$ has weak transverse secondary flow, with a large influence area away from the endwall. The resukts show that the increase of the exit angle weakens the transverse secondary flow and increases its influence area.

Figure 17 shows the total pressure loss coefficient from 0.9b to 1.1b cross sections and the endwall streamline for different exit angles. It is seen that the increase of the exit angle weakens the passage vortex and increases its influence area. The separation of the suction surface moves back with the increase of the exit angle. Compared with Figure 11, it is found that the common point is that the large flow coefficient limits the influence area of the passage vortex.

5. Conclusion

In this paper, the influence law of the variation of the stagger angle and exit angle of the cascade on the flow coefficient and loss coefficient is investigated by numerical simulant. The effects of flow coefficient on high-pressure turbine aerodynamic performance is analyzed. The main findings are as follows:

(1) The flow coefficient is influenced by the stagger angle and the exit angle. The flow coefficient is decreased from 0.478 to 0.374 as the stagger angle is changed from 44.2° to 56.2° and from 0.630 to 0.341 as the exit angle is changed from 63° to 75°. The flow coefficient is more sensitive to the exit angle

(2) The total pressure loss coefficient is decreased with the increase of the stagger angle. At large stagger angle, on the one hand, the adverse pressure gradient affects a large area, resulting in large boundary layer losses. On the other hand, the adverse pressure gradient is small, resulting in weak but large transverse secondary flow. In addition, the increase in stagger angle also enhances the influence of passage vortices and endwall secondary flow

(3) The total pressure loss coefficient is increased and then decreased with the increase of the exit angle. At large exit angle, the adverse pressure gradient is small with a small influence area, resulting in low boundary layer losses and weak but large transverse secondary flow. The strength of the passage vortex is decreased, while the influence area is increased

Nomenclature

α: Stagger angle (°)
B: Axial chord(m)
c_x: Axial velocity(m/s)

Y: Total pressure loss coefficient
$p_{t,\text{out}}$: Outlet total pressure (Pa)
C_p: Pressure coefficient
μ: Dynamic viscosity (Pa•s)
ρ: Density of air (kg•m^{-3})
$T_{t,\text{in}}$: Inlet total temperature (K)
β: Exit angle (°)
φ: Flow coefficient
u: Blade velocity at mid-span (m/s)
$p_{t,\text{in}}$: Inlet total pressure (Pa)
$p_{s,\text{out}}$: Outlet static pressure (Pa)
ϕ: Dissipation function
δ: Boundary layer thickness(m)
θ: Boundary layer momentum thickness (m)

Data Availability

The numerical data used to support the findings of this study are included within the article.

Conflicts of Interest

The author(s) declare(s) that they have no conflicts of interest.

Acknowledgments

The authors acknowledge the financial support provided by Natural Science Foundation of China (No.52106041, No. 52076053), Postdoctoral Special Assistant in Heilongjiang Province(LBH-TZ2109), China Postdoctoral Science Foundation funded project (2021 M690823), National Science and Technology Major Project (No. 2019-II-0010-0030), and Natural Science Fund for Excellent Young Scholars of Heilongjiang Province [No. YQ2021E023].

References

[1] D. Liu and R. Cheng, "Current status and development direction of aircraft power technology in the world," *Journal of Beijing University of Aeronautics and Astronautics*, vol. 28, no. 5, p. 490, 2002.

[2] W. Koop, "The integrated high performance turbine engine technology program," *International Society for Air Breathing Engines*, vol. 97, p. 7175, 1997.

[3] L. M. Wright and J. C. Han, "Enhanced internal cooling of turbine blades and vanes," *The Gas Turbine Handbook*, vol. 4, pp. 1–5, 2006.

[4] L. Meng, H. Li, G. Xie, Z. Tao, and Z. Zhou, "Film cooling performance on pressure side of turbine blade with different number of hole rows under rotating state," *Aerospace Science and Technology*, vol. 126, p. 107569, 2022.

[5] W. Du, L. Luo, Y. Jiao, S. Wang, X. Li, and B. Sunden, "Heat transfer in the trailing region of gas turbines - A state-of-the-art review," *Applied Thermal Engineering*, vol. 199, p. 117614, 2021.

[6] W. Du, L. Luo, S. Wang, and B. Sunden, "Film cooling in the trailing edge cutback with different land shapes and blowing ratios," *International Communications in Heat and Mass Transfer*, vol. 125, p. 105311, 2021.

[7] S. Lu, Q. Deng, P. M. Ligrani, H. Jiang, and Q. Zhang, "Effects of coolant and wall temperature variations on impingement jet array thermal performance," *Numerical Heat Transfer, Part A: Applications*, vol. 79, no. 1, pp. 68–82, 2021.

[8] W. Zhou, Q. Deng, W. He, J. He, and Z. Feng, "Conjugate heat transfer analysis for composite cooling structure using a decoupled method," *International Journal of Heat and Mass Transfer*, vol. 149, p. 119200, 2020.

[9] J. Liu, W. Du, S. Hussain, G. Xie, and B. Sundén, "Endwall film cooling holes design upstream of the leading edge of a turbine vane," *Numerical Heat Transfer, Part A: Applications*, vol. 79, no. 3, pp. 222–245, 2021.

[10] R. J. Howell, H. P. Hodson, V. Schulte et al., "Boundary layer development in the BR710 and BR715 LP turbines—the implementation of high-lift and ultra-high-lift concepts," *Journal of Turbomachinery*, vol. 124, no. 3, pp. 385–392, 2002.

[11] R. J. Howell, O. N. Ramesh, H. P. Hodson, N. W. Harvey, and V. Schulte, "High lift and aft-loaded profiles for low-pressure turbines," *Journal of Turbomachinery*, vol. 123, no. 2, pp. 181–188, 2001.

[12] S. F. Smith, "A simple correlation of turbine efficiency," *The Aeronautical Journal*, vol. 69, no. 655, pp. 467–470, 1965.

[13] D. G. Ainley and G. Mathieson, "Performance of Axial-Flow Turbines," *ARCHIVE Proceedings of the Institution of Mechanical Engineers, 1847-1982 (vols 1-196)*, vol. 159, no. 1, p. 230-24, 1948.

[14] H. Craig and H. Cox, "Performance estimation of axial flow turbines," *Proceedings of the Institution of Mechanical Engineers*, vol. 185, no. 1, pp. 407–424, 1970.

[15] S. C. Kacker and U. Okapuu, "A mean line prediction method for axial flow turbine efficiency," *Journal of Engineering for Power*, vol. 104, no. 1, pp. 111–119, 1982.

[16] J. D. Coull and H. P. Hodson, "Blade loading and its application in the mean-line design of low pressure turbines," *Journal of Turbomachinery*, vol. 135, no. 2, pp. 21–32, 2013.

[17] I. Zhdanov, S. Staudacher, and S. Falaleev, "An advanced usage of meanline loss systems for axial turbine design optimization," in *ASME Turbo Expo 2013: Turbine Technical Conference and Exposition*, San Antonio, Texas, USA, June 2013.

[18] R. Va' Squez, D. Cadrecha, and D. Torre, "High stage loading low pressure turbines: a new proposal for an efficiency chart," in *ASME Turbo Expo 2003, collocated with the 2003 International Joint Power Generation Conference*, Atlanta, Georgia, USA, June 2003.

[19] H. P. Wang, S. J. Olson, R. J. Goldstein, and E. R. G. Eckert, "Flow visualization in a linear turbine cascade of high performance turbine blades," *Journal of Turbomachinery*, vol. 119, no. 1, pp. 1–8, 1997.

[20] X. Qu, Y. Zhang, X. Lu, J. Zhu, and Y. Zhang, "Unsteady influences of blade loading distribution on secondary flow of ultra-high-lift LPT," *Aerospace Science and Technology*, vol. 96, p. 105550, 2020.

[21] X. Qu, Y. Zhang, X. Lu, G. Han, Z. Li, and J. Zhu, "Effects of periodic wakes on the endwall secondary flow in high-lift low-pressure turbine cascades at low Reynolds numbers," *Proceedings of the Institution of Mechanical Engineers, Part G: Journal of Aerospace Engineering*, vol. 233, no. 1, pp. 354–368, 2019.

[22] M. Sinkwitz, B. Winhart, D. Engelmann, F. di Mare, and R. Mailach, "On the periodically unsteady interaction of

wakes, secondary flow development, and boundary layer flow in an annular low-pressure turbine Cascade: an experimental investigation," *Journal of Turbomachinery*, vol. 141, no. 9, article 091001, 2019.

[23] B. Winhart, M. Sinkwitz, D. Engelmann, F. Di Mare, and R. Mailach, "On the periodically unsteady interaction of wakes, secondary flow development and boundary layer flow in an annular lpt cascade: Part 2—numerical investigation," in *ASME Turbo Expo 2018: Turbomachinery Technical Conference and Exposition*, Oslo, Norway, June 2018.

[24] A. P. Darji, B. D. Baloni, and C. S. Mistry, "Numerical Investigations on Effect of Inflow Parameters on Development of Secondary Flow Field for Linear LP Turbine Cascade," in *ASME 2021 Gas Turbine India Conference*, December 2021.

[25] H. Tsujita and M. Kaneko, "Effects of Shock Wave Development on Secondary Flow Behavior in Linear Turbine Cascade at Transonic Condition," in *Proceedings of the ASME Turbo Expo 2020: Turbomachinery Technical Conference and Exposition*, 2020.

[26] D. Simoni, V. Yepmo, P. Zunino, M. Ubaldi, D. Lengani, and F. Bertini, "Turbine Cascade Profile Loss Sensitivity to Incoming Wake Parameters: Effects of Reduced Frequency, Wake Momentum Defect and Axial Gap," in *Proceedings of the ASME Turbo Expo 2019: Turbomachinery Technical Conference and Exposition*, Phoenix, Arizona, USA, 2019.

[27] H. Kodama, K. I. Funazaki, K. Ito, R. Ikehata, and Y. Koda, "A Method for Estimating Profile Loss of Low Pressure Turbine Blades from the Low Speed Cascade Test Data," in *Proceedings of the ASME Turbo Expo 2019: Turbomachinery Technical Conference and Exposition*, Phoenix, Arizona, USA, 2019.

[28] V. Dossena, G. D'Ippolito, and E. Pesatori, "Stagger angle and pitch-chord ratio effects on secondary flows downstream of a turbine cascade at several off-design conditions," in *ASME Turbo Expo 2004: Power for Land, Sea, and Air*, pp. 1429–1437, Vienna, Austria, June 2004.

[29] T. Behr, *Control of Rotor Tip Leakage and Secondary Flow by Casing Air Injection in Unshrouded Axial Turbines*, Diss, ETH Zurich, 2007.

[30] W. Du, L. Luo, S. Wang, and X. Zhang, "Heat transfer characteristics in a pin finned channel with different dimple locations," *Heat Transfer Engineering*, vol. 41, no. 14, pp. 1232–1251, 2020.

[31] L. M. Seguí, L. Y. M. Gicquel, F. Duchaine, and J. de Laborderie, "Importance of boundary layer transition in a high-pressure turbine cascade using LES," in *ASME Turbo Expo 2018: Turbomachinery Technical Conference and Exposition*, Oslo, Norway, June 2018.

[32] M. E. Nakhchi, S. W. Naung, and M. Rahmati, "DNS of secondary flows over oscillating low-pressure turbine using spectral/hp element method," *International Journal of Heat and Fluid Flow*, vol. 86, p. 108684, 2020.